Atmospheric
Chemistry
and Physics

Supplement of

Sea spray emissions from the Baltic Sea: comparison of aerosol eddy co-variance fluxes and chamber-simulated sea spray emissions

Julika Zinke et al.

Correspondence to: Julika Zinke (julika.zinke@su.se) and Ernst Douglas Nilsson (douglas.nilsson@aces.su.se)

Supplement

S1   Diurnal cycles

Figure S20 illustrates the diurnal variations of several variables during both campaigns, including the ambient particle concentration, in situ fluxes, wind speed, stability, friction velocity, turbulent kinetic energy, roughness length, neutral drag coefficient, wave age, significant wave height, seawater and air temperature, sensible and latent heat flux, dissolved oxygen, and chlorophyll-α concentration.

In general, diurnal cycles in surface layer turbulence are driven by vertical and horizontal winds, temperature, and water vapor. The diurnal cycle of air temperature is influenced by radiation and turbulent heat fluxes. Deviations from this cycle can occur due to air advection driven by synoptic weather. The energy absorbed by the sea is distributed in the surface layer through turbulent transport in the water. This is in contrast to continental surfaces, where absorption of radiation leads to local warming and more pronounced diurnal temperature cycles. As a result, diurnal cycles in temperature are less distinct over oceans. During both campaigns, air temperature peaked during daytime, while seawater temperature remained relatively constant.

The stability remained close to neutral, with $\frac{z}{L}$ ranging from -0.1 to +0.1, as shown in Fig. S9), but it was slightly stable during the night and early morning hours (see Fig. S20b). The friction velocity, $u*$, reached a minimum value of just below 0.1 m s^{-1} at midnight and a peaked at about 0.3 m s^{-1} at noon (see Fig. S20c). The turbulent kinetic energy reached its maximum in the afternoon (see Fig. S20c). The diurnal cycle of the significant wave height, H_s, showed an increase from 0.6 m in the morning to just below 1 m in the afternoon (see Fig. S20e). The surface roughness, z_0, followed the same diurnal cycle as H_s, with peak values of 0.16 mm in the afternoon when the highest waves were observed and the smallest roughness of 0.036 mm in the morning when the waves were smallest (see Fig. S20d). The diurnal cycle of the wave age had the opposite shape compared to H_s, with a median minimum from 0.7 to 0.9 from noon to afternoon and maximum median values from 1.1 to 1.5 during the rest of the day (see Fig. S20e). Therefore, the highest waves were also the youngest. Finally, the neutral drag coefficient, CD_N, followed the same average diurnal cycle as H_s and z_0, with a morning minimum at $0.99 \cdot 10^{-3}$ and an afternoon peak at $1.27 \cdot 10^{-3}$ (see Fig. S20d).

The ambient aerosol number concentrations measured on Östergarnsholm exhibit a slight increase during nighttime, although there is a large variation in the data (see Fig. S20a). This contrasts with the findings of Long et al. (2014), who observed a peak in particle concentration during daytime. Aerosols in the Baltic region can also have anthropogenic origins, originating from industries and populated areas around the coast as well as from ship exhaust. During night and morning hours, stratification is often stable, particularly in May, which results in a shallower surface layer, less mixing and consequently higher aerosol concentrations.

The EC aerosol flux measured on Östergarnsholm exhibited a maximum during daytime, which is related to the peak in wind
30   speed around midday (see Fig. S20a). Nilsson et al. (2021) measured EC aerosol fluxes at the Kalmar strait in the Baltic Sea
and observed a similar diurnal pattern in EC aerosol fluxes and wind speed.

The concentration of dissolved oxygen during the Oceania cruise in May showed a minimum just after 12:00 and higher
concentrations around 06:00 and 18:00 (see Fig. S20h). During the Electra campaign, the dissolved oxygen concentration
had its minimum during the early morning hours (around 06:00) and was highest during midday. A similar diurnal cycle in
35   dissolved oxygen concentration measured during the Electra campaign was observed by Hultin et al. (2011). The concentration
of chlorophyll-α during the Electra campaign also showed a minimum during the early morning hours and increased slightly
in the afternoon (see Fig. S20h). Unfortunately, there were not enough data points for the chlorophyll-α measurements during
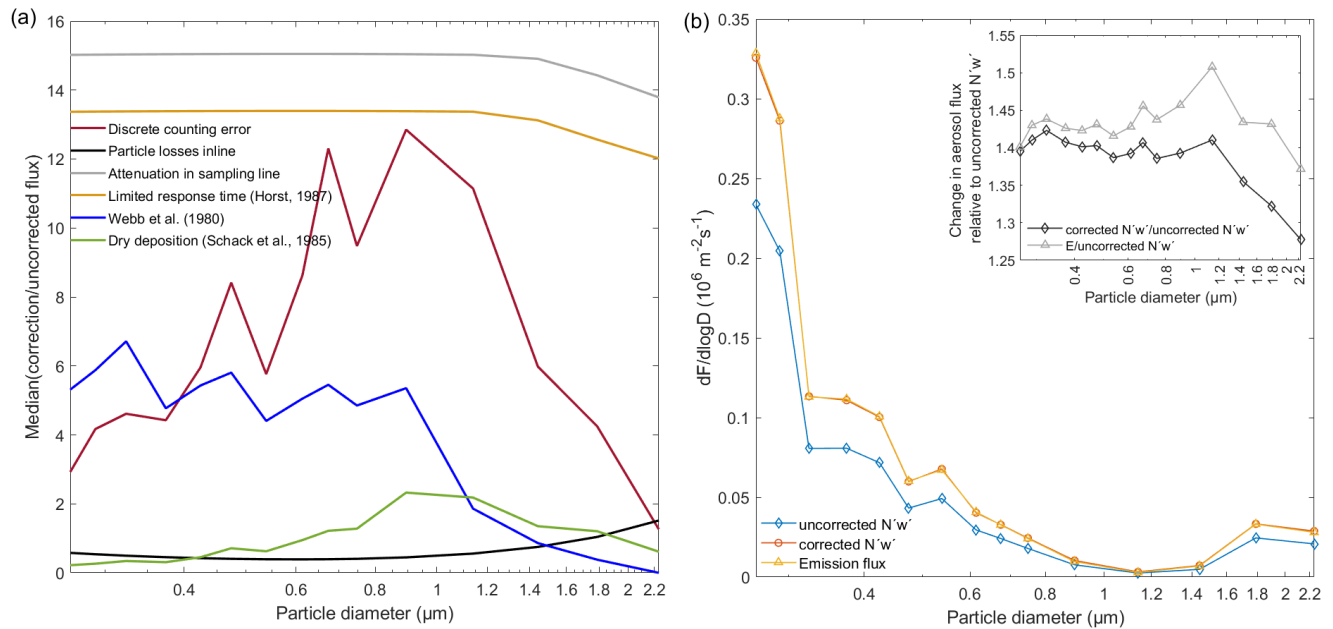the Oceania campaign.

S2   Figures

Figure S1. (a) Size resolved relative errors (errors/uncorrected net flux) for signal attenuation in the sampling line, limited response time,
particle losses in the sampling line, the Webb correction, discrete counting error and modelled aerosol dry deposition flux. (b) Size-resolved
uncorrected median net flux, fully corrected median net flux and median emission flux. The inset shows the ratio of the fully corrected to
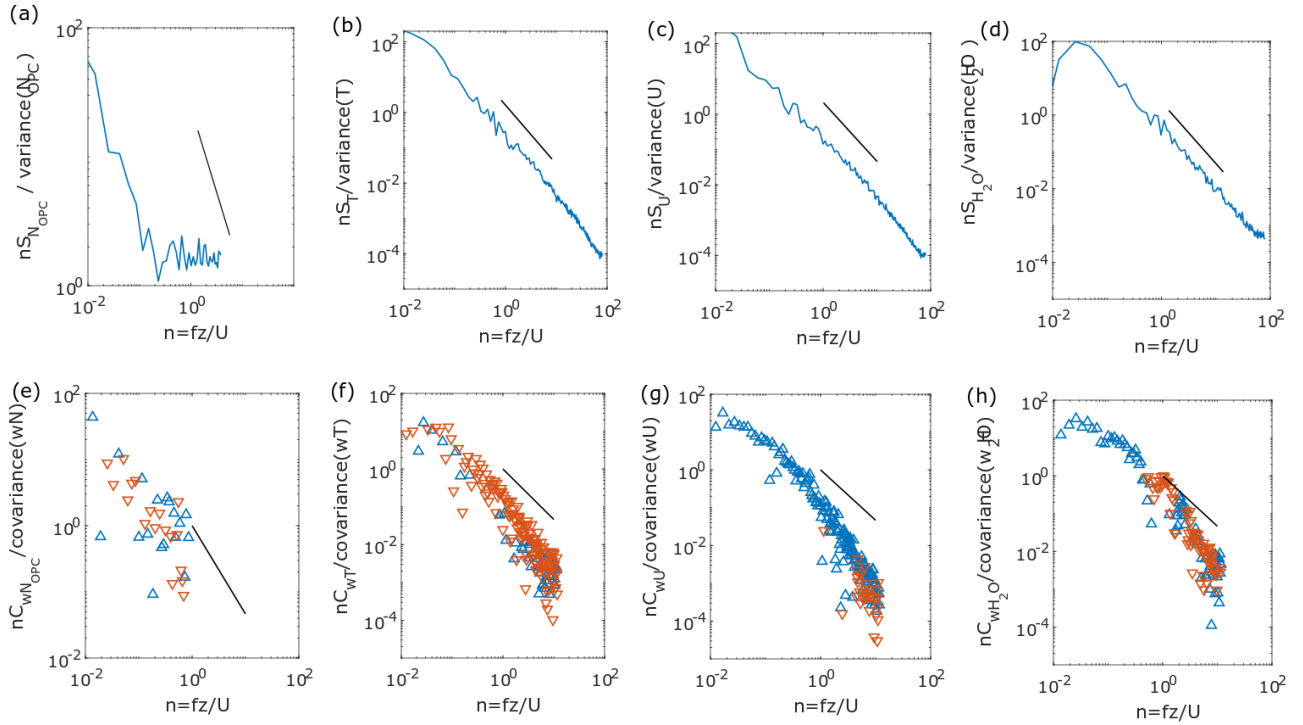uncorrected net flux and the ratio of emission flux to uncorrected net flux.

Figure S2. Normalised power spectra for (a) particle concentration measured with the OPC, (b) temperature, (c) horizontal wind, and (d) water vapor (H_2O) plotted against the dimensionless frequency. The black lines indicate the -5/3 slope, which represents the theoretical decay within the inertial subrange. Normalised co-spectra of vertical wind (e) particle concentration measured with the OPC, (f) temperature, (g) horizontal wind, and (h) water vapor (H_2O) plotted against the dimensionless frequency. The black lines indicate the -4/3 slope that is representative of the theoretical decay within the inertial subrange. The orange, downward pointing triangles represent negative covariances, while the blue upward pointing triangles represent positive covariances.
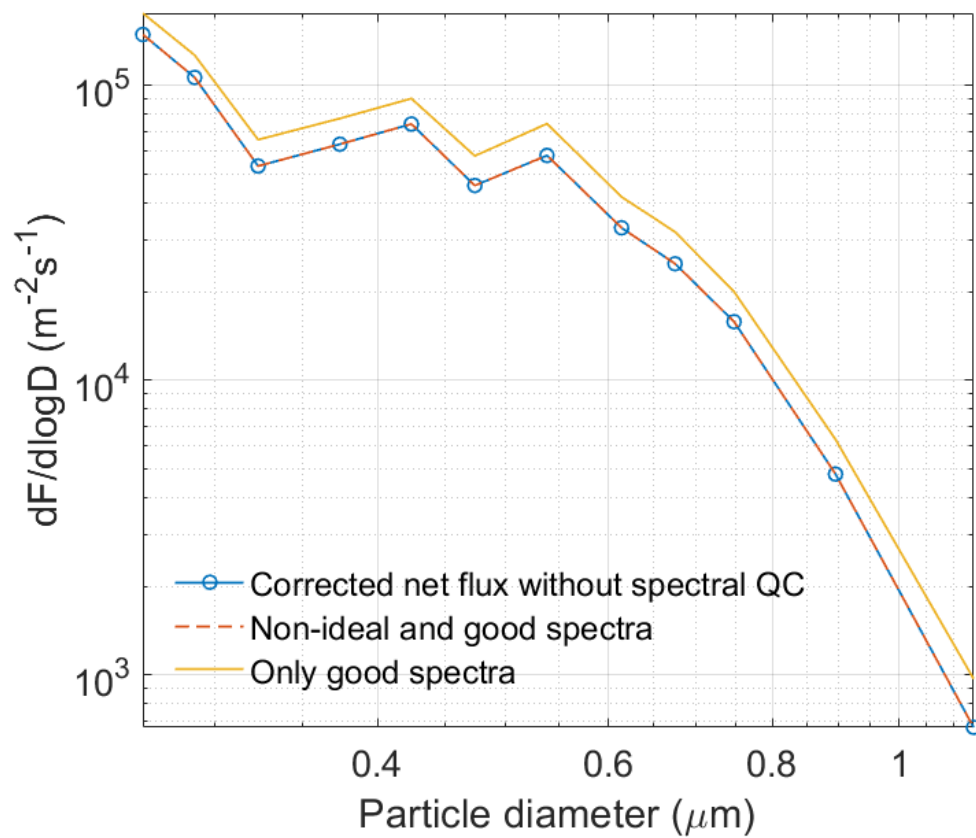
Figure S3. Effect of spectral analysis on the emission flux size distribution measured on Östergarnsholm.
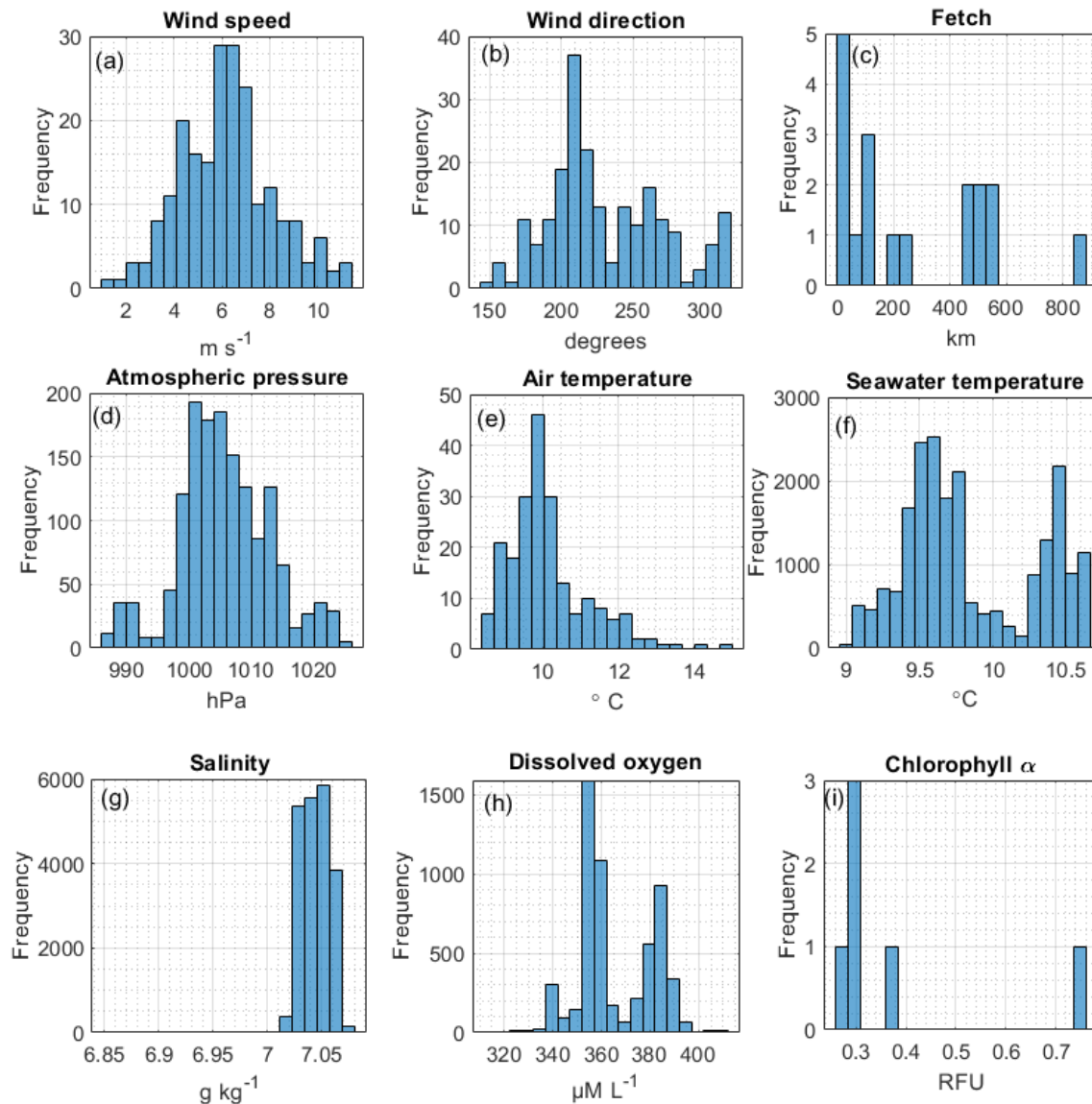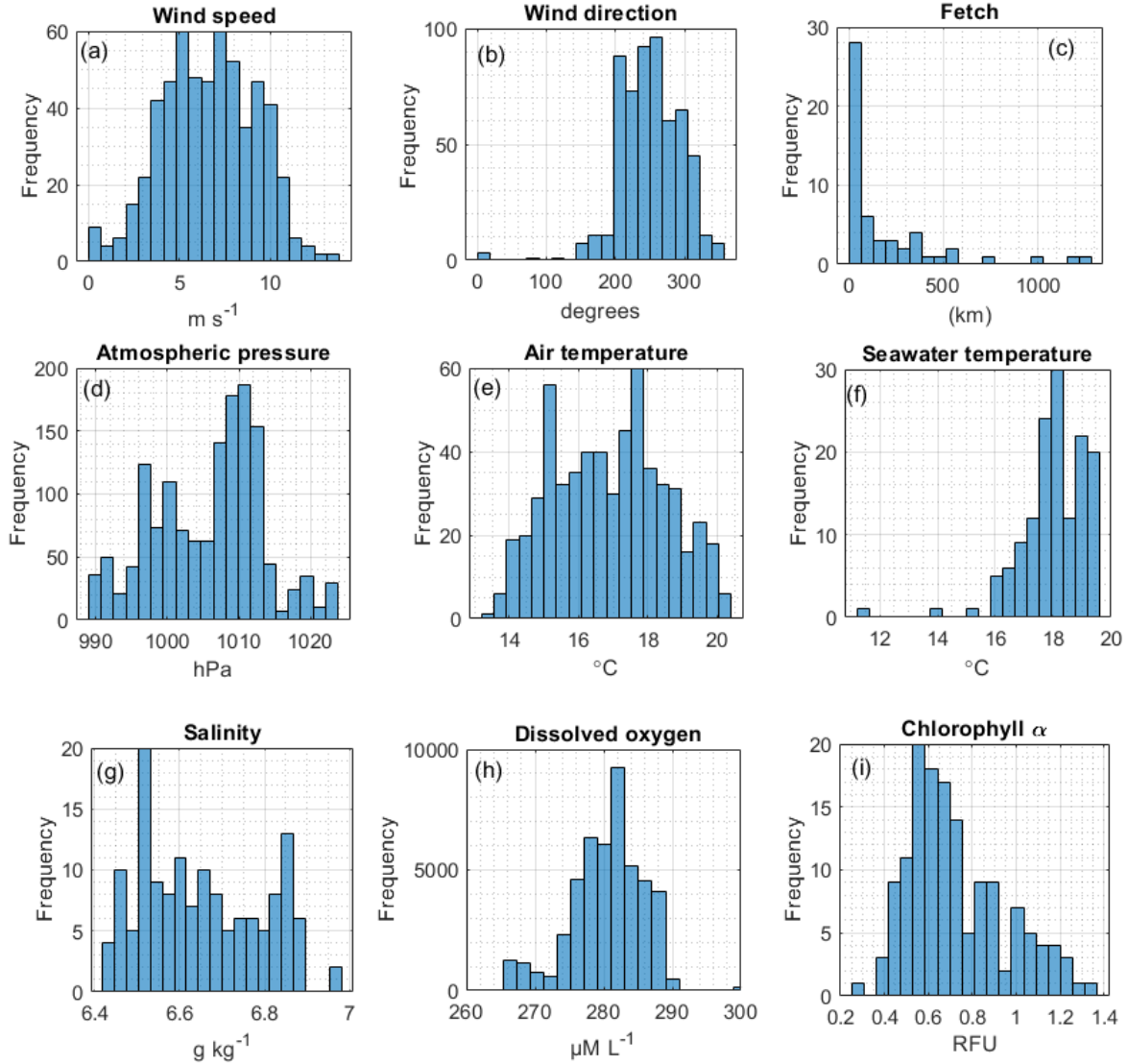
Figure S4. Overview of the synoptical situation during the Oceania campaign, (a) wind speed, (b) wind direction, (c) fetch, (d) atmospheric pressure, (e) air temperature, (f) seawater temperature, (g) seawater salinity, (h) dissolved oxygen concentration in the seawater and (i) concentration of chlorophyll-α in reference fluorescence units (RFU) in the seawater.
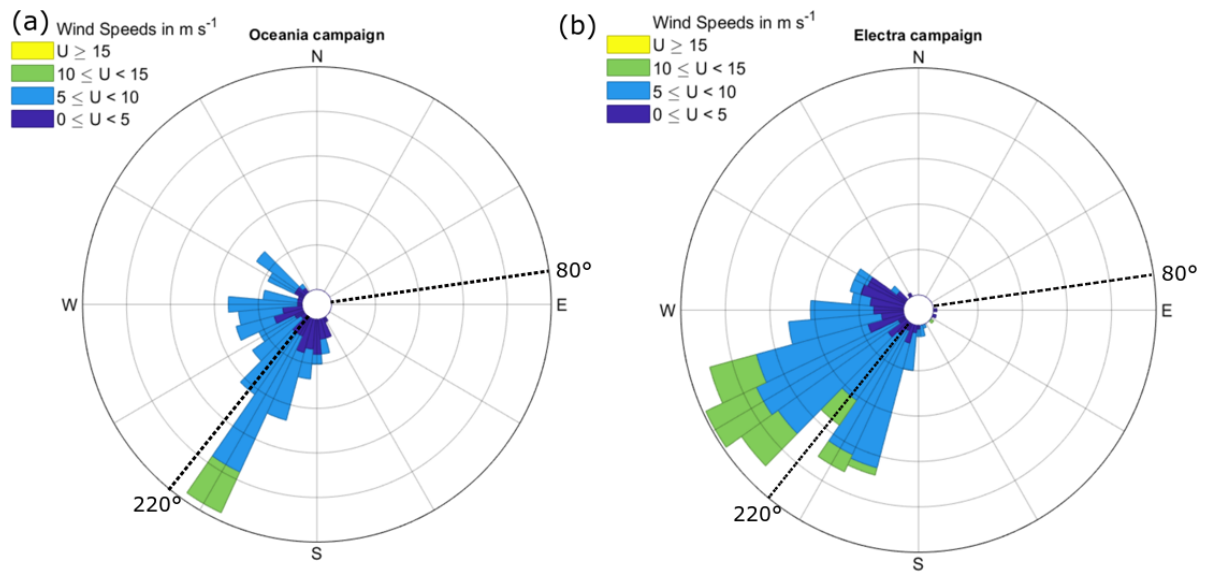
Electra campaign

Figure S5. Overview of the synoptical situation during the Electra campaign, (a) wind speed, (b) wind direction, (c) fetch, (d) atmospheric pressure, (e) air temperature, (f) seawater temperature, (g) seawater salinity, (h) dissolved oxygen concentration in the seawater and (i) concentration of chlorophyll-α in reference fluorescence units (RFU) in the seawater.

Figure S6. Prevailing wind speeds and directions during the Oceania campaign in May (a) and Electra campaign in August (b). The dashed lines mark the open sea sector.
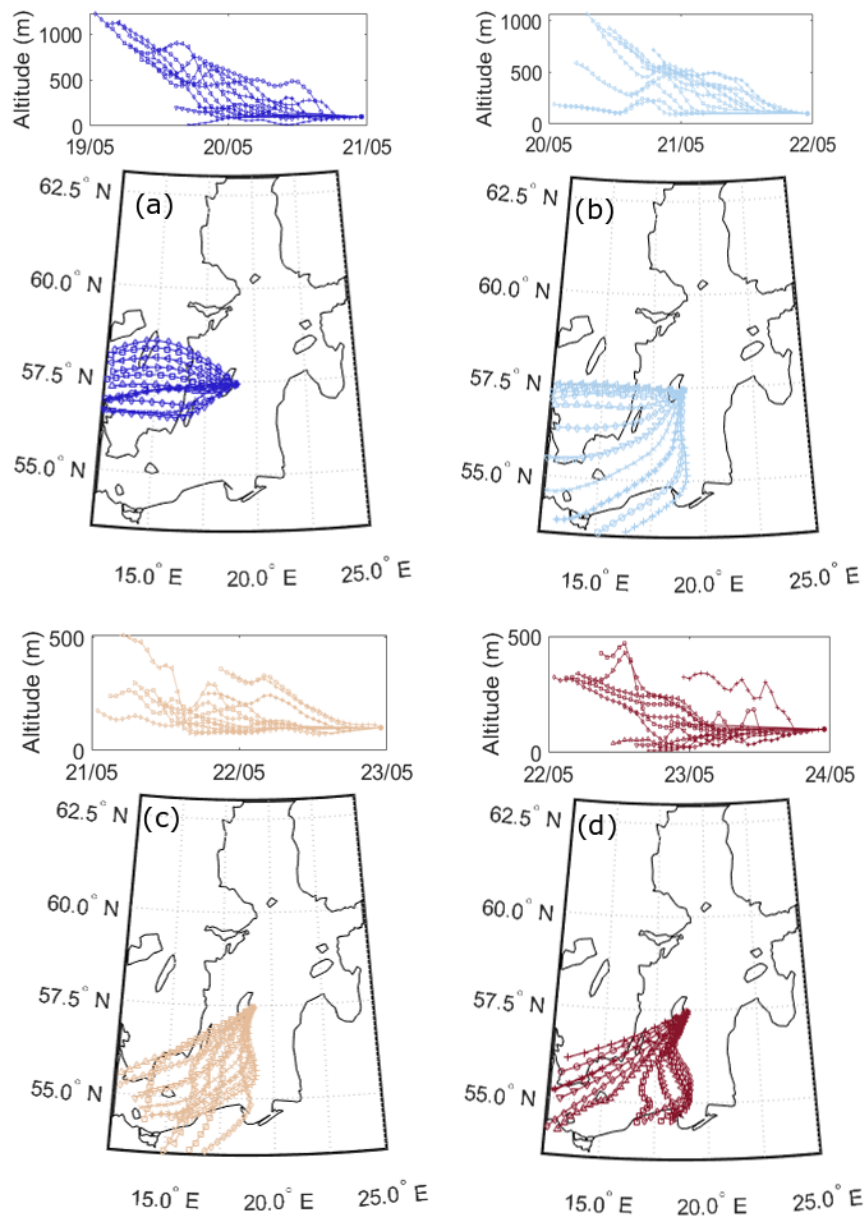
Figure S7. Hysplit 24-hour backward trajectories (every second hour) for sampling days when Oceania was located close to the station.
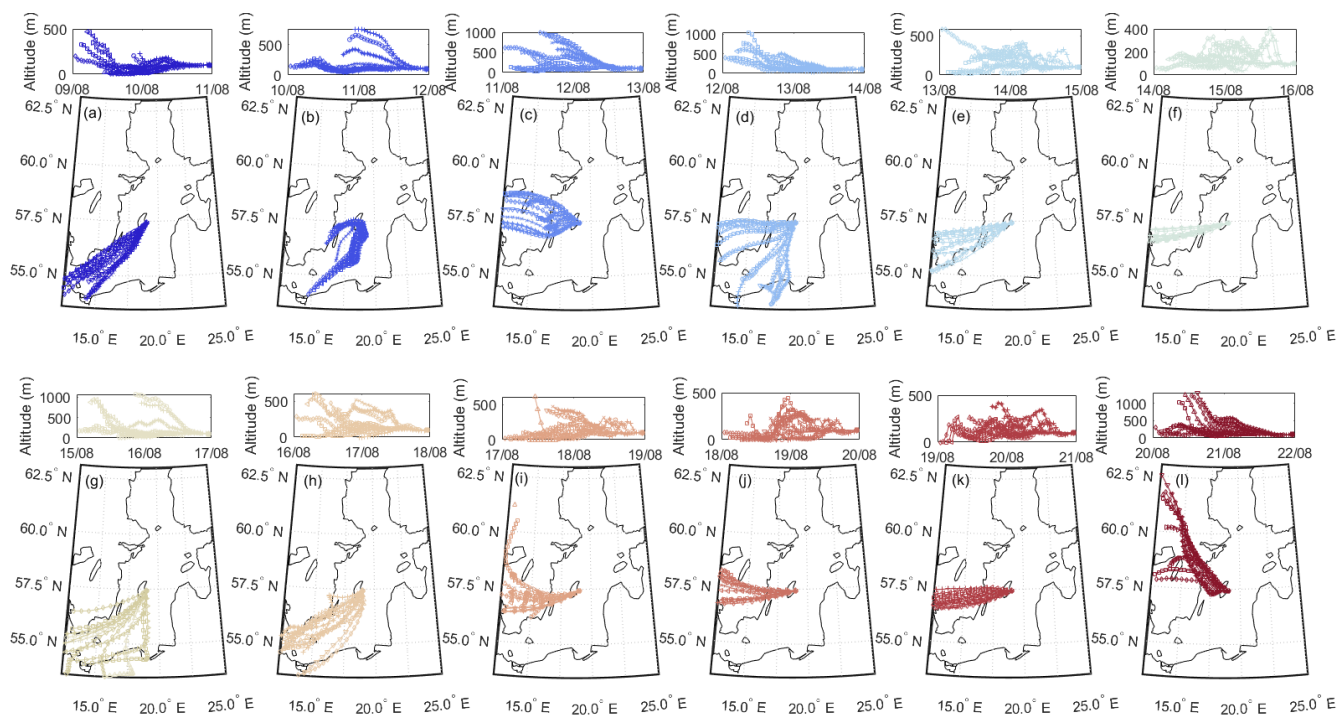
Figure S8. Hysplit 24-hour backward trajectories (every second hour) for sampling days when Electra was located close to the station.
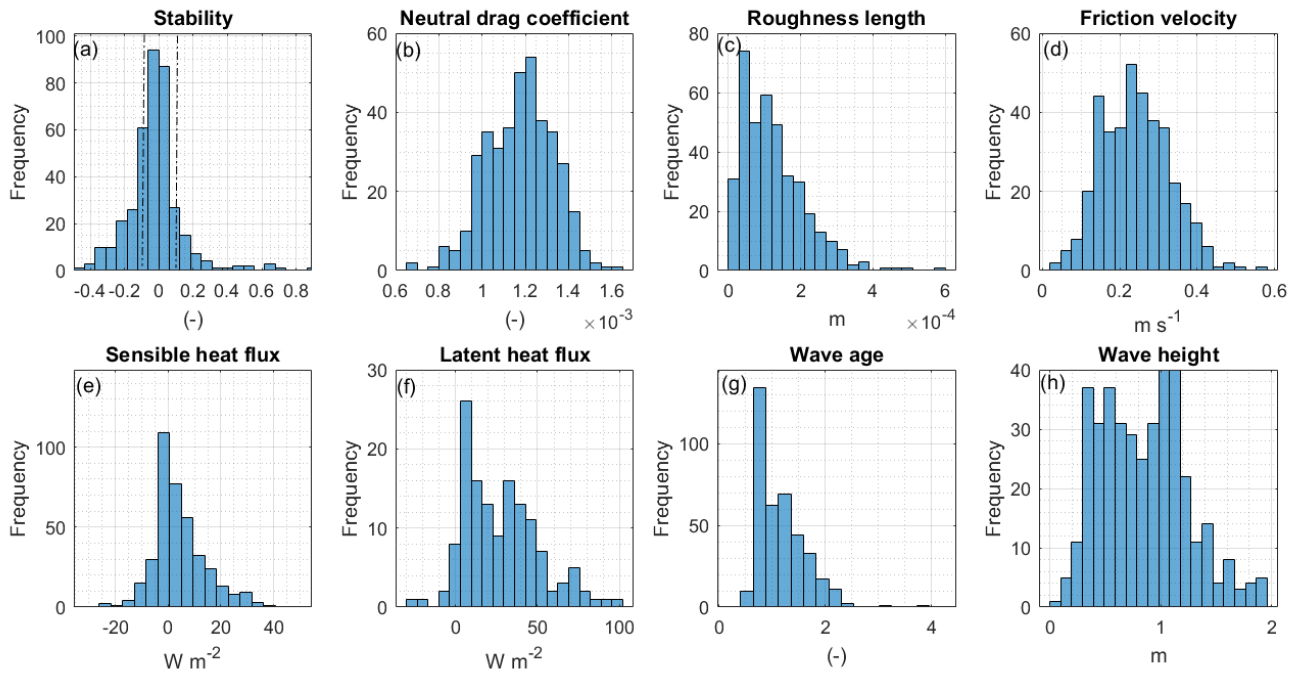
Figure S9. Histograms of micrometeorological parameters for campaigns combined. (a) Stability, (b) neutral drag coefficient, (c) roughness length, (d) friction velocity, (e) sensible heat flux, (f) latent heat flux, (g) wave age and (h) wave height. Only data from the open sea sector is shown. The dashed line in panel (a) indicates stable ($\frac{z}{L} > 0.1$), neutral ($-0.1 < \frac{z}{L} < 0.1$) and unstable ($-0.1 < \frac{z}{L}$) conditions.
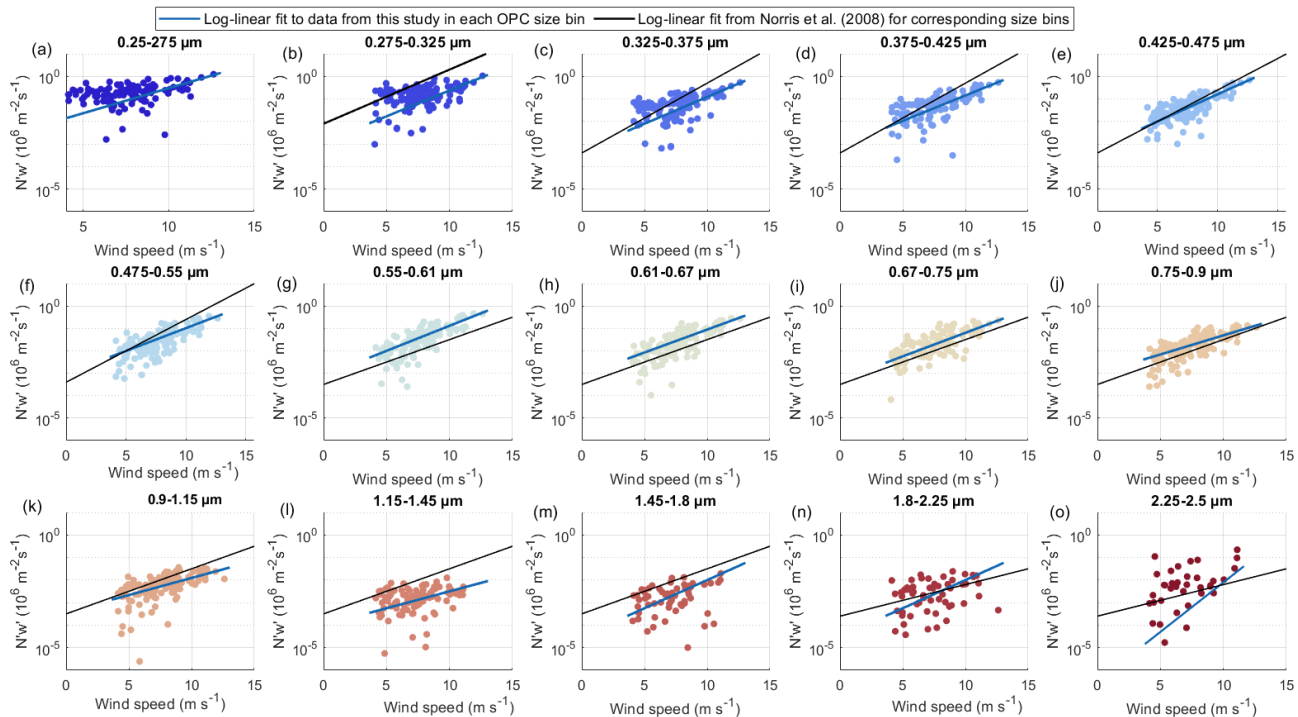
Figure S10. (a)-(o) Dependence of the in situ EC fluxes in different size bins on wind speed with log-linear fits (the coefficients for each fit are provided in Fig. S11. The fits for aerosol EC fluxes from Norris et al. (2008) are added for matching size bins.
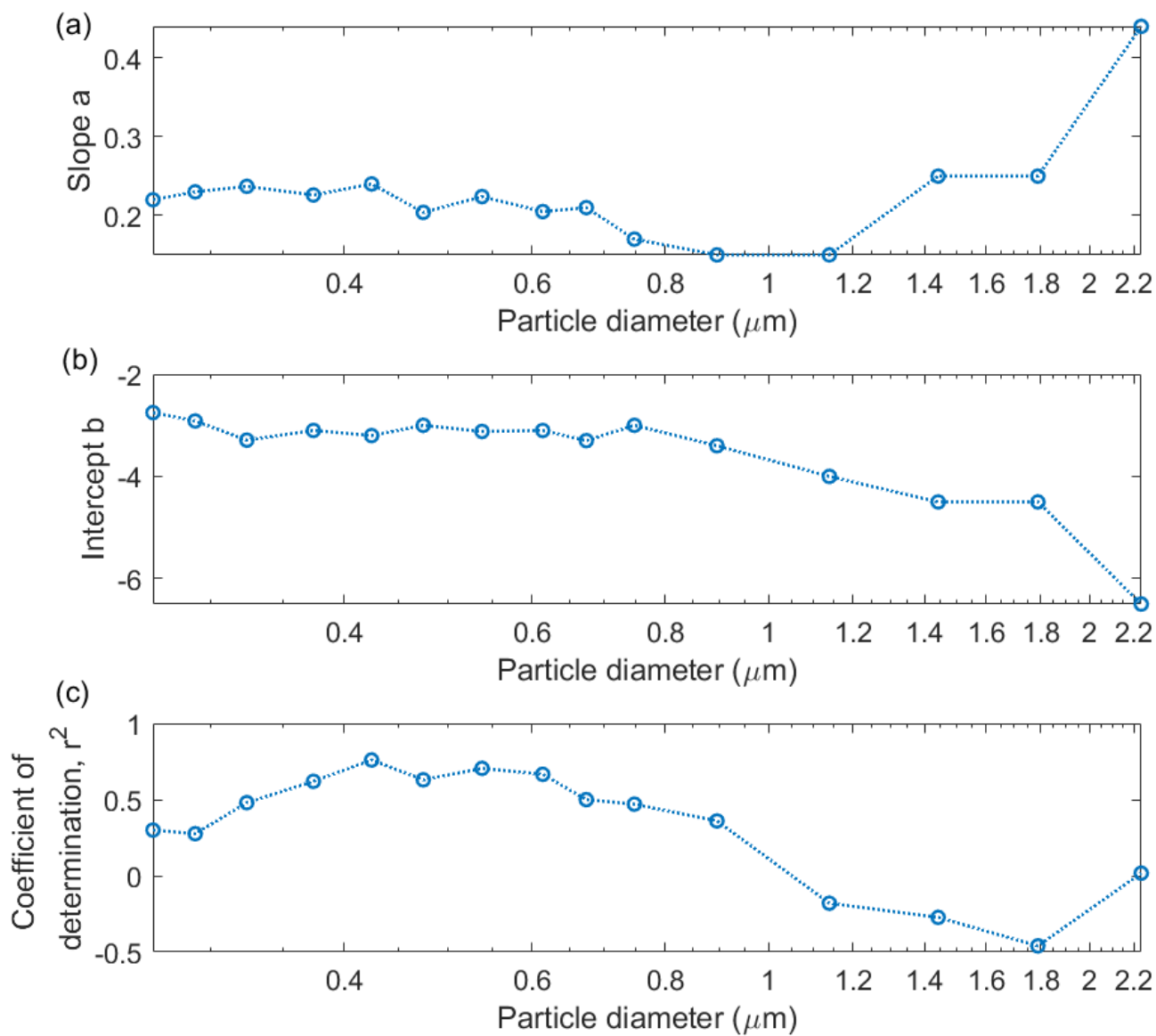
11

Figure S11. (a) Slope a, (b) intercept b and (c) coefficient of determination r^2 for the size-resolved log-linear fits with wind speed (equation 12) for both emission and EC fluxes.
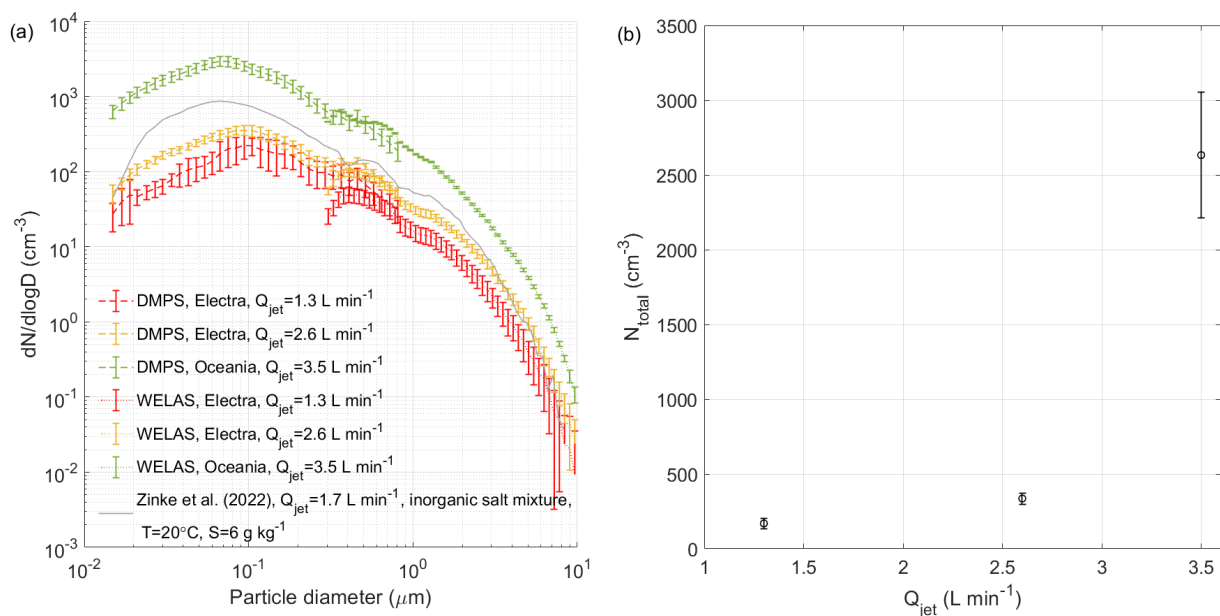
Figure S12. (a) Overlap between the number size distributions measured by the DMPS and WELAS for different jet flow rates and (b) total concentrations of particles measured in the headspace of the sea spray simulation chamber at different jet speeds. Values are given as mean and standard deviation. The WELAS reaches $100\,\%$ counting efficiency for particles with diameters larger than 0.3 μm (Rosati et al., 2015), which is why the size distributions measured by the DMPS and WELAS were combined at 0.35 μm.
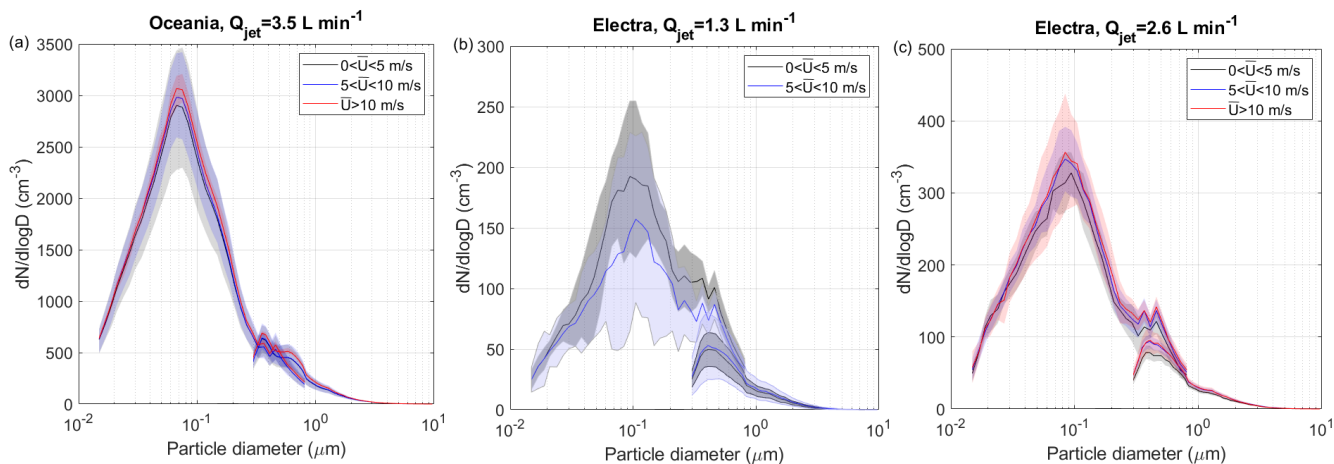
Figure S13. Effect of wind speed on the particle concentration in the head space of the sea spray simulation chamber a) at a jet flow of 3.5 L min^{-1} speed during the Oceania campaign, b) at a jet flow of 1.3 L min^{-1} during the Electra campaign and c) at a jet flow of 2.6 L min^{-1} during the Electra campaign. Values are depicted as mean and standard deviation. mean and standard deviation. At particle diameters below 0.3 µm, the counting efficiency is less than 100 % (Rosati et al., 2015), which is why the WELAS was only used for particles diameters > 0.35 µm.
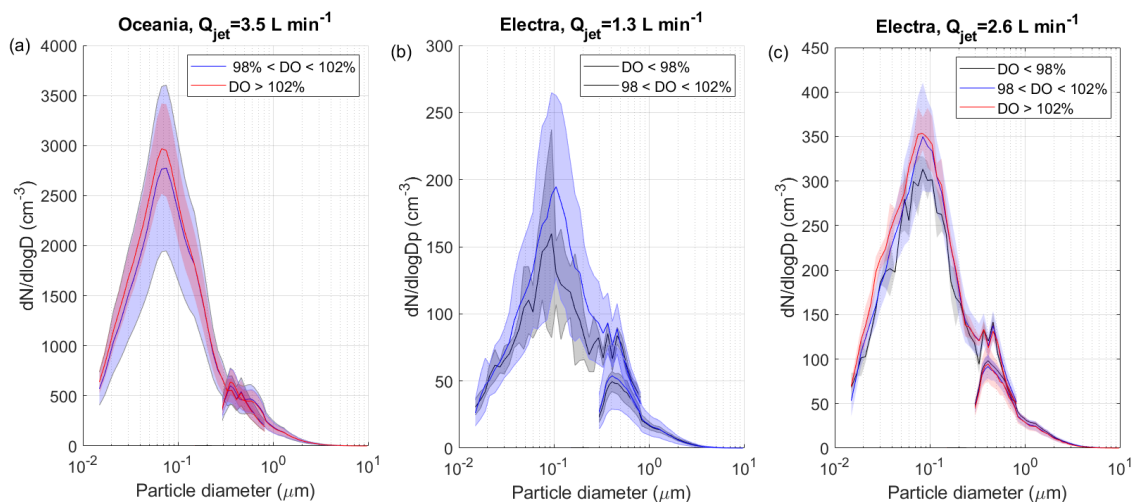

Figure S14. Effect of dissolved oxygen (DO) saturation on the particle concentration in the head space of the sea spray simulation chamber a) at a jet flow of 3.5 L min^{-1} during the Oceania campaign, b) at a jet flow of 1.3 L min^{-1} during the Electra campaign and c) at a jet flow of 2.6 L min^{-1} during the Electra campaign. Values are depicted as mean and standard deviation.
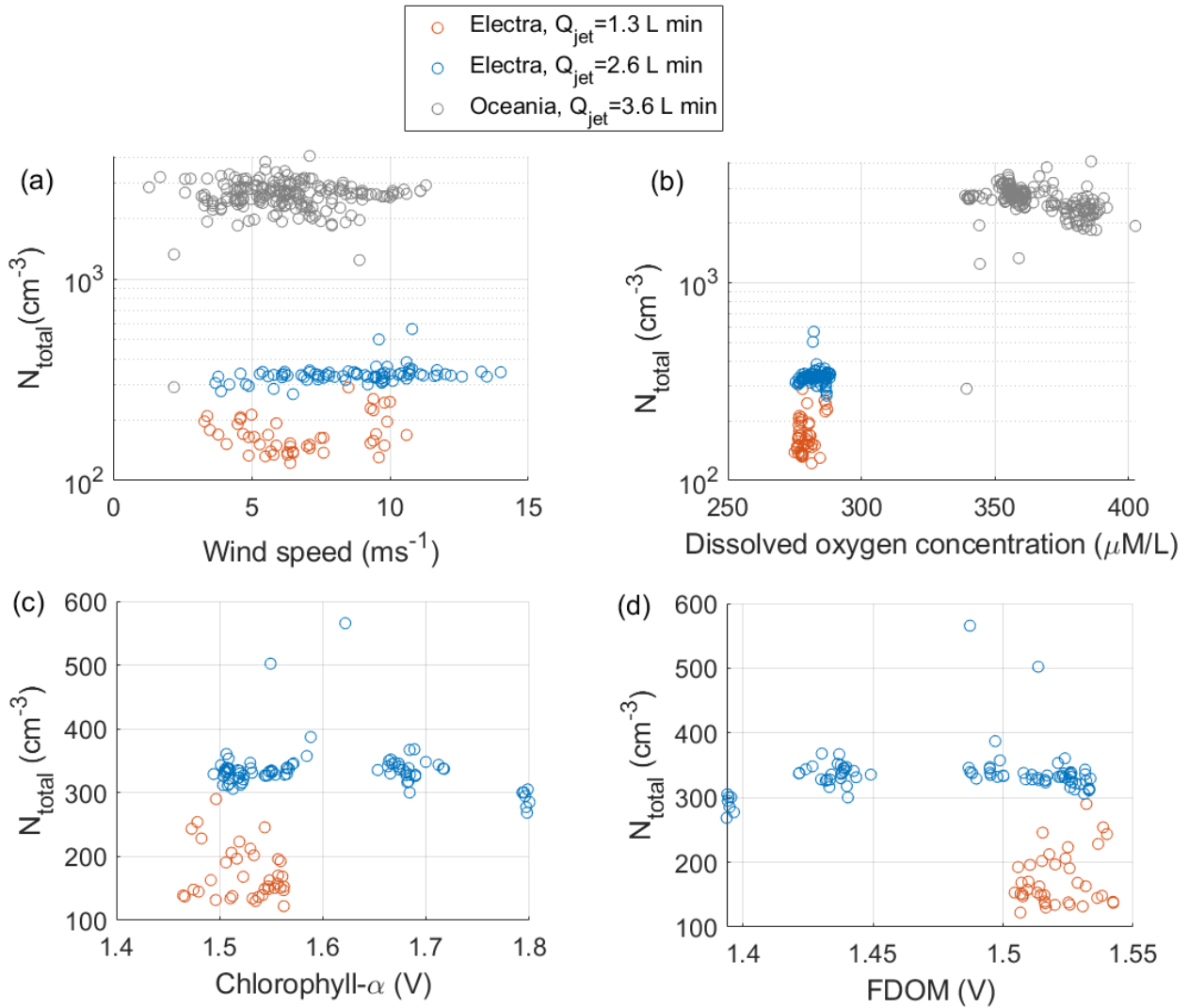
Figure S15. Dependence of particle concentration in the headspace of the sea spray simulation chamber during on (a) wind speed, (b) dissolved oxygen concentration, (c) chlorophyll-a and (d) FDOM. The chlorophyll-a and FDOM concentrations are given in volt (V) measured by the fluorometer.
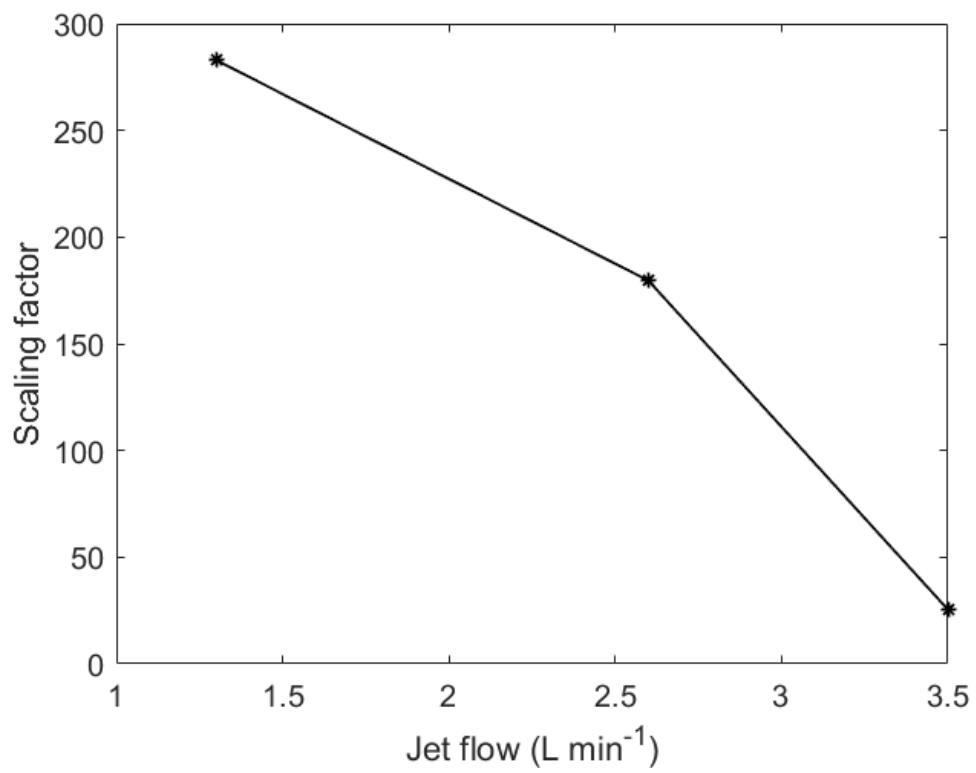
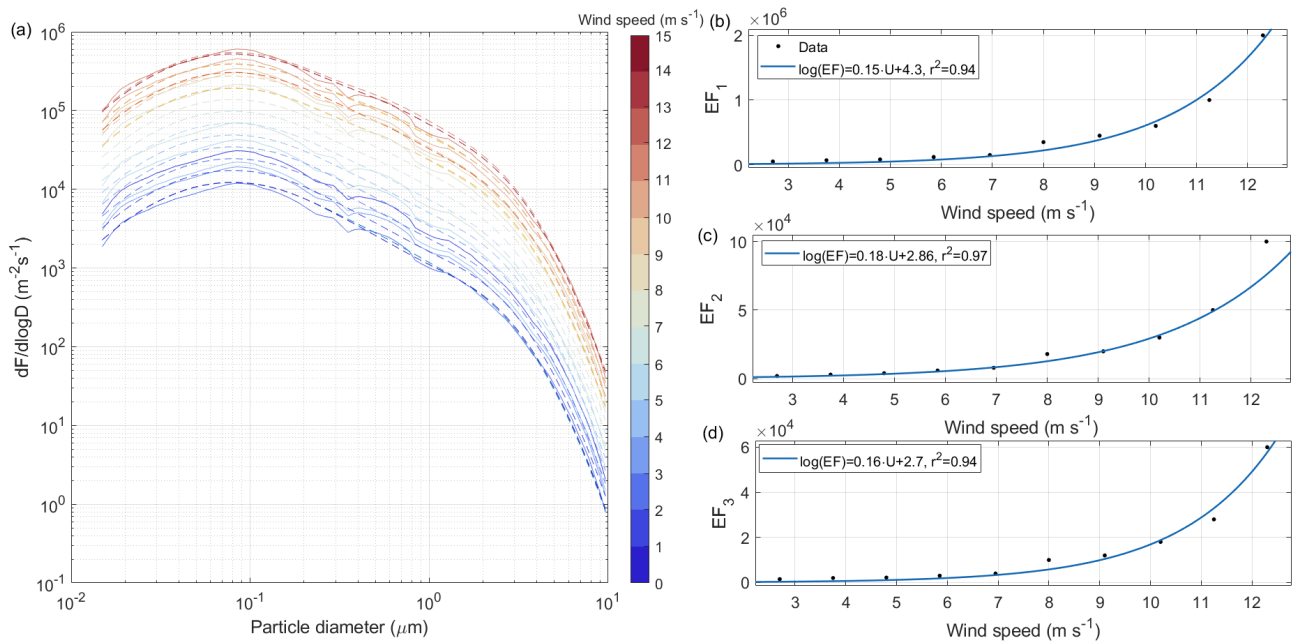**Figure S16.** Dependence of the scaling factor on jet flow rate.

Figure S17. (a) Measured (solid lines) and parameterised (dashed lines) emission flux in dependence on wind speed, (b)-(d) log-linear fits to the emission magnitude in each mode with increasing wind speed.
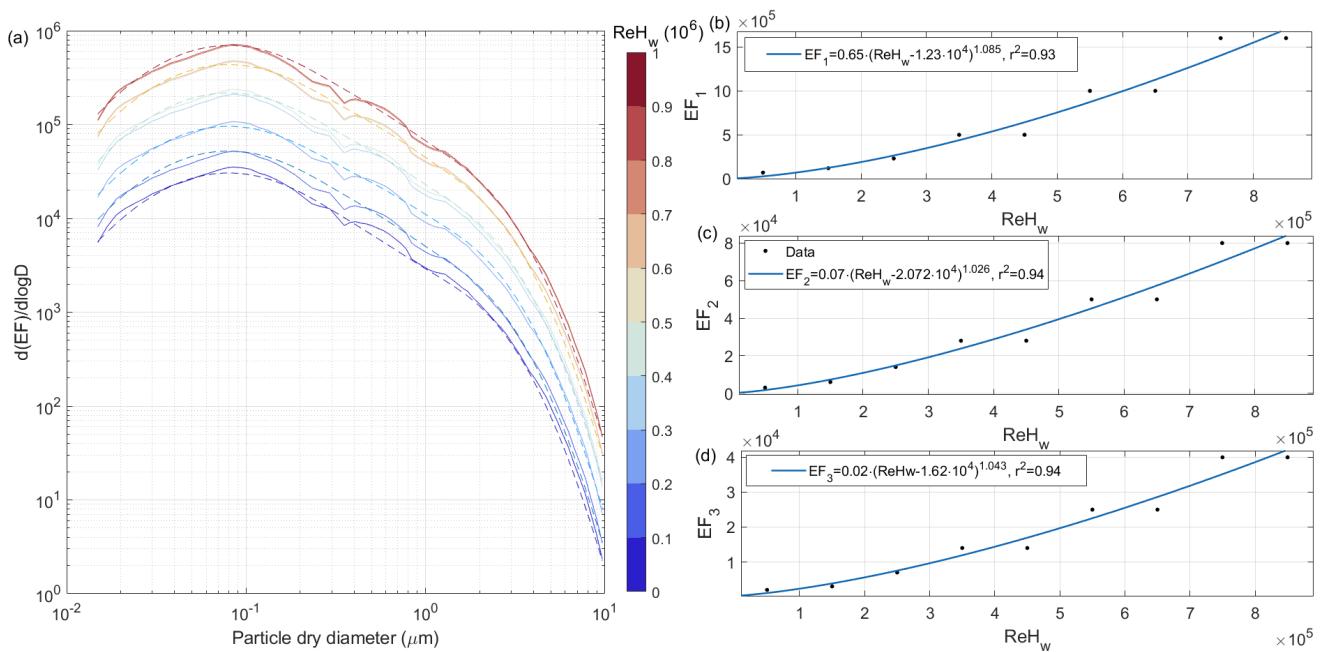

Figure S18. (a) Measured (solid lines) and parameterised (dashed lines) emission flux in dependence on wave Reynolds number, (b)-(d) Fits to the emission magnitude in each mode with increasing wave Reynolds number.
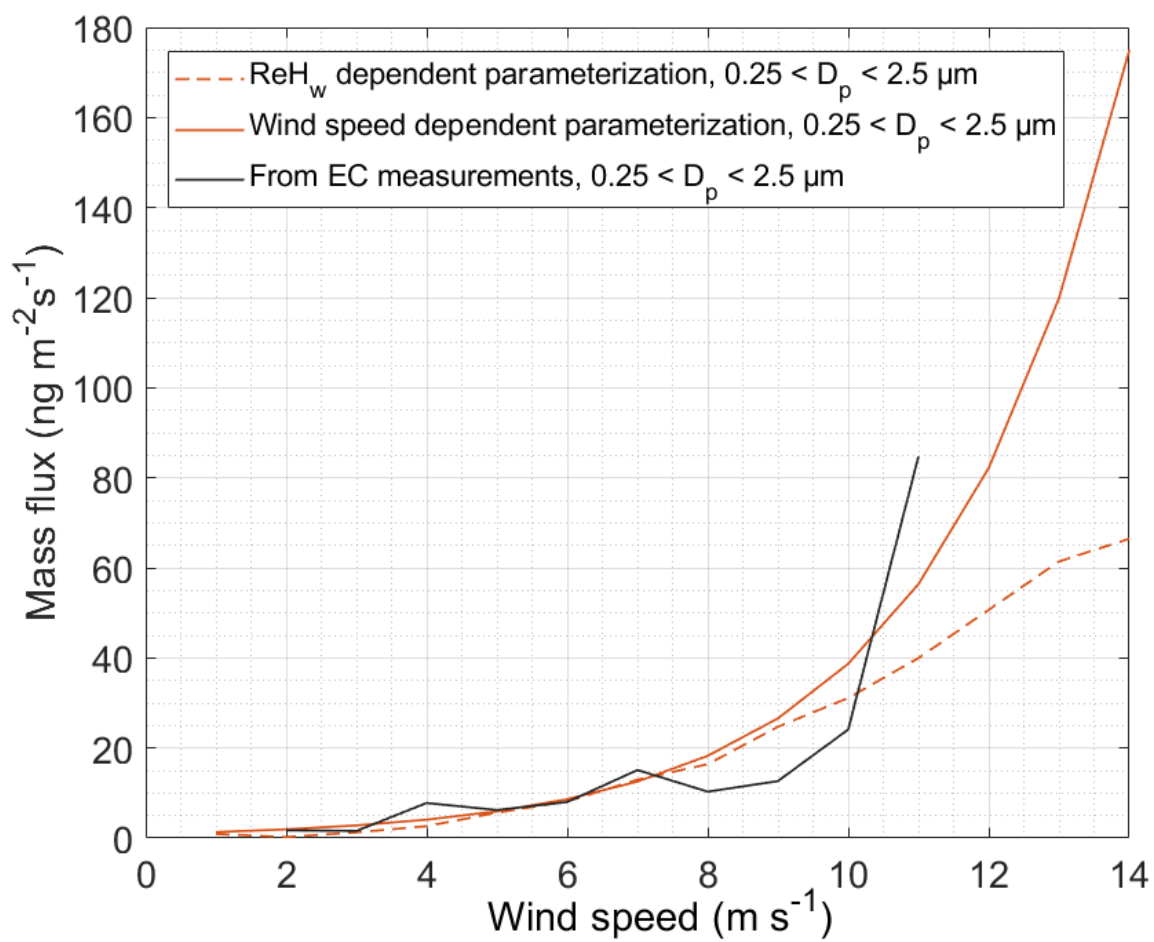
Figure S19. Comparison of mass flux estimates from the wave Reynolds number dependent and wind speed dependent parameterizations with mass flux estimates from the in-situ measurements.
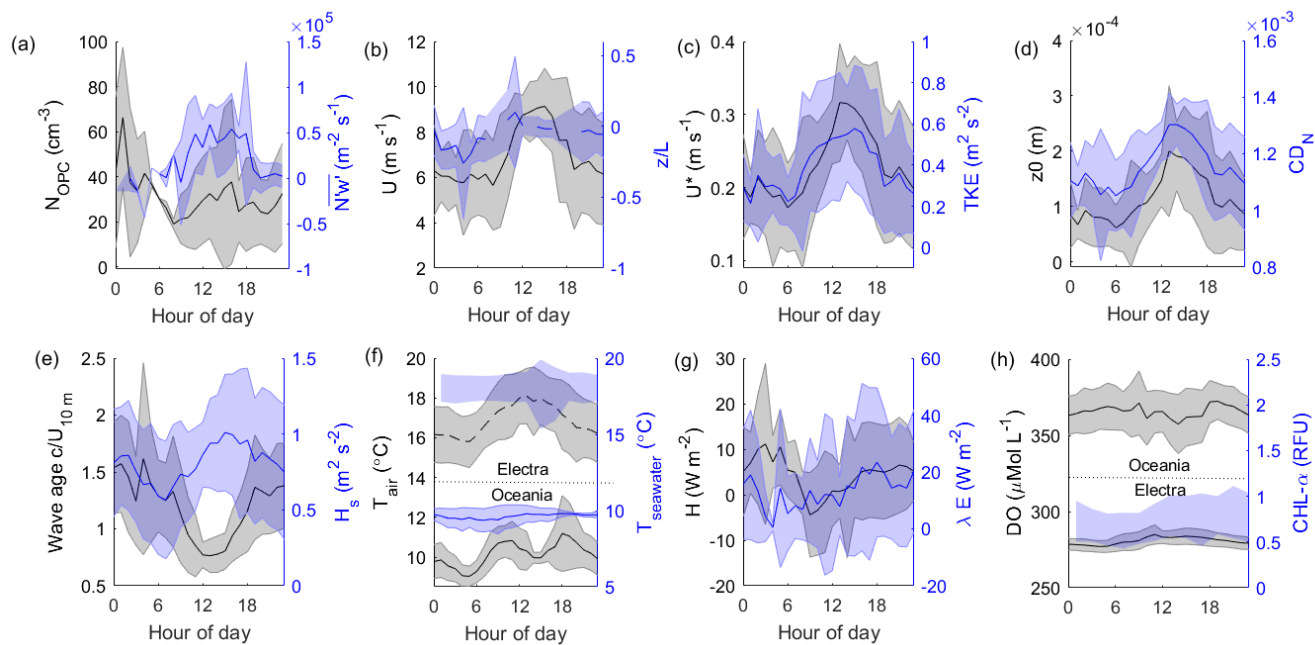
Figure S20. Diurnal cycles (presented as mean and standard deviation) for the Oceania and Electra campaign: (a) ambient particle concentrations and EC fluxes measured on Östergarnsholm, (b) wind speed and stability, (c) friction velocity and turbulent kinetic energy, (d) Roughness length and neutral drag coefficient, (e) wave age and wave height, (f) air temperature and seawater temperature, (g) sensible heat flux and latent heat flux and (h) dissolved oxygen and chlorophyll-α concentration for both campaigns. For T_{air}, $T_{seawater}$ and DO concentration, the dirunal cycles are shown separately for the two campaigns. For the Oceania campaign, there are not enough data points of chlorophyll-α for a diurnal cycle.

References

Hultin, K. A. H., Krejci, R., Pinhassi, J., Gomez-Consarnau, L., Mårtensson, E. M., Hagström, A., and Nilsson, E. D.: Aerosol and bacterial emissions from Baltic seawater, Atmospheric Research, 99, 1–14, https://doi.org/10.1016/j.atmosres.2010.08.018, 2011.

Long, M., Keene, W., Kieber, D., Frossard, A., Russell, L., Maben, J., Kinsey, J., Quinn, P., and Bates, T.: Light-enhanced primary marine aerosol production from biologically productive seawater, Geophys. Res. Lett., 41, 2661–2670, 2014.

Nilsson, E. D., Hultin, K. A., Mårtensson, E. M., Markuszewski, P., Rosman, K., and Krejci, R.: Baltic Sea Spray Emissions: In Situ Eddy Covariance Fluxes vs. Simulated Tank Sea Spray, Atmosphere, 12, 274, https://doi.org/10.3390/atmos12020274, 2021.

Norris, S. J., Brooks, I. M., de Leeuw, G., Smith, M. H., Moerman, M. M., and Lingard, J. J.: Eddy covariance measurements of sea spray particles over the Atlantic Ocean, Atmos. Chem. Phys., 8, 555–563, https://doi.org/10.5194/acp-8-555-2008, 2008.

Rosati, B., Wehrle, G., Gysel, M., Zieger, P., Baltensperger, U., and Weingartner, E.: The white-light humidified optical particle spectrometer (WHOPS) – a novel airborne system to characterize aerosol hygroscopicity, Atmos. Meas. Tech., 8, 921–939, https://doi.org/10.5194/amt-8-921-2015, 2015.